THE ASTROPHYSICAL JOURNAL, 325:644–650, 1988 February 15

HIGH-RESOLUTION IMAGING OF THE DOUBLE QSO 2345+007: EVIDENCE FOR SUBCOMPONENTS[1]

J.-L. NIETO,[2] S. ROQUES,[2] A. LLEBARIA,[3] CH. VANDERRIEST,[4] G. LELIÈVRE,[5]
S. DI SEREGO ALIGHIERI,[6,7] F. D. MACCHETTO,[8] AND M. A. C. PERRYMAN[9]

Received 1987 June 23; accepted 1987 August 4

ABSTRACT

We have observed, at the CFH telescope with the time-resolved imaging mode of the ESA Photon Counting Detector, the field of the double QSO 2345+007 in the UV band. Integrated images have a 0".55–0".60 resolution; by using recentering and selection algorithms, we obtain images reaching 0".4 resolution. From several lines of evidence, we show that component B is resolved and elongated in a direction almost perpendicular to the AB direction.

A further improvement in resolution has been achieved by applying image restoration techniques. The results show that component B is made of two subcomponents of roughly equal intensity, 0".36 apart. The line of their centers makes a slight ($\sim 12°$) angle with the AB direction. At least one of the two subcomponents, B2, is elongated in a direction perpendicular to the AB direction and is responsible for the observed elongation of component B.

The magnitude difference between A and B is 1.70 mag. A comparison with previously published data suggests some variability in the system. This result and the specific configuration described above give new support for the gravitational lens hypothesis: A and the two subcomponents of B, B1 and B2, are different images of the same source quasar, with B2 being better interpreted as an unresolved multiple component image than a really extended object. The AB splitting would result from the action of a single galaxy and its cluster as a whole, while the $B_1 B_2$ splitting requires the action of another $5 \times 10^{10}\ M_\odot$ galaxy.

Subject headings: gravitational lenses — image processing — quasars

I. INTRODUCTION

Since the first discovery of a convincing candidate for gravitational image splitting of the light from a distant quasar (Walsh, Carswell, and Weymann 1979), several other cases have been proposed. These candidates illustrate the large variety of appearances that this basic phenomenon can produce.

For 2345+007 (Weedman *et al.* 1982), the large separation of the two components A and B, allied to the lack of any obvious deflecting body, makes a simple gravitational lens model difficult. Very deep CCD imaging by Tyson *et al.* (1986) failed to reveal any object (either a galaxy or a cluster) responsible for the lensing, so that a "nonluminous" mass of $10^{13}\ M_\odot$ is required to explain the large separation of the two images. The gravitational lens interpretation has recently even been questioned (Bahcall, Bahcall, and Schneider 1986).

Two further observations of this system ought to be mentioned:

1) Features in the spectrum of component B and the marginally redder color of B suggest the presence of a faint underlying galaxy (Tyson *et al.* 1986);

2) Sol *et al.* (1984) found marginal evidence for component B to be broader than component A on images having a resolution poorer than 1".3, but did not confirm this from better resolution images in a note added in proof in the same paper.

Clearly, new observational data with the highest possible resolution are required for a better understanding of 2345+007. We report here the results of high-resolution imaging of this field in the UV band. This study is the first astrophysical application of a strategy (Nieto and Lelièvre 1985) aiming to provide high-resolution imaging. In this method, short-exposure images obtained with a photon-counting system in a time-resolved imaging mode from a high-resolution site are processed using recentering and selection algorithms, so that several images are obtained with different resolutions and different signal-to-noise ratios. Image restoration techniques are then applied to these images, a compromise between resolution and signal-to-noise ratio yielding the best image that it is possible to derive during a given observing period with given observing conditions. The recentering and selection algorithms, based on the maximum correlation function, are presented in Nieto, Llebaria, and di Serego Alighieri (1987, hereafter Paper I). The image restoration technique is discussed in detail in Lannes *et al.* (1987*a*, *b*) and Roques (1987). The deconvolved images are accompanied by an error analysis which provides an estimate of the stability of the solution.

Section II deals with our observational approach. In § III, we discuss both the integrated images and those derived from recentering and selection algorithms, the latter reaching 0".4 resolution (FWHM). Emphasis is given to the evidence for

[1] Observations were made with the CFH Telescope, operated by the National Research Council of Canada, the Centre National de la Recherche Scientifique of France, and the University of Hawaii.

[2] Observatoire du Pic-du-Midi et de Toulouse, Unité Associée au CNRS No. 285, Toulouse, France.
[3] Laboratoire d'Astronomie Spatiale, Marseille, France.
[4] Observatoire de Paris, Section d'Astrophysique de Meudon, France.
[5] Canada-France-Hawaii Telescope Corporation, USA.
[6] The Space Telescope European Coordinating Facility, Federal Republic of Germany.
[7] Affiliated to the Astrophysics Division, Space Science Department, European Space Agency.
[8] Space Telescope Science Institute, USA.
[9] European Space Agency, ESTEC, The Netherlands.

component B being resolved. The restored images are described in § IV: they reach 0".24 resolution (FWHM). A physical interpretation is proposed in § V. Conclusions are given in § VI.

II. OBSERVATIONS: THE APPROACH

The observations were made on 1984 October 16 at the Cassegrain focus of the CFH telescope with the ESA Photon Counting Detector (PCD), the scientific prototype of the Faint Object Camera for the Space Telescope (di Serego Alighieri, Perryman, and Macchetto 1985). In conjunction with the exceptional resolution achievable at the CFH site, the UV sensitivity of the camera provided a good opportunity to try to detect new images of the proposed gravitationally lensed QSO 2345+007, either very embedded with the other images such as in the case of PG 1105+080 (Foy, Bonneau, and Blazit 1985), or simply too faint to have been detected previously. We used a UG1 filter transmitting from the atmospheric cutoff to 4000 Å. The observations are described in Table 1. The pixel size along the scanning direction is 0".175, and it was checked on other fields observed during the same run. This gives an 80" × 80" field of view for the 512 × 512 format of the instrument. A typical UG1 128 × 128 image centered on the field of 2345+007 is presented in Figure 1 (Plate 22).

The very good resolution estimated on focus stars (FWHM ~ 0".5) prompted us to use the Time Resolved Imaging Mode (TRIM) of the Camera (di Serego Alighieri and Perryman 1986), where images are recorded at the frame rate of 30 ms and loaded onto magnetic tapes covering ~1000 s exposure time each. Since the tapes were analyzed independently, each one is considered as a separate exposure in Table 1. Our goal was to improve the resolution of the images with off-line image recentering and selection algorithms (Paper I). These algorithms monitor the motion and the blurring of the image during short integration times, ranging from 0.1 s to several seconds. The chosen integration time is determined from the event input rate necessary for a reliable monitoring, following the shape of the object used for this purpose and its contrast above sky level (Thouvenot 1987). The algorithms search for the maximum correlation between the short-exposure images and the total integrated image, used as an unsharp mask. Several long-exposure images can be then obtained by this procedure after recentering the short-exposure images and by selecting the highest resolution ones. This approach allows one to obtain the best images from a given observing period, unlike real-time corrections (e.g., Thompson and Ryerson 1983; Thompson 1984) where the target resolution of the image must be decided *a priori* by the observer. It requires, however, an extensive reduction procedure. Our package (Paper I) is implemented on the VAX 780 of the Centre Français du Telescope Spatial in Marseilles, and works within the MIDAS software system developed at ESO (Banse *et al.* 1983).

TABLE 1

OBSERVATIONS[a]

Number	Exposure Time (s)	Mode	Filter	FWHM[b]
1.....	100	Integrated	UG1	0".60
2.....	1000	TRIM	UG1	0.63
3.....	1000	TRIM	UG1	0.60
4.....	1000	TRIM	UG1	0.53
5.....	1000	Integrated	UG1	0.53

[a] 1984 Oct 16.
[b] FWHM of the integrated images.

In our field of view, since there is no bright star available for image monitoring, we used for this purpose component A which looks quite stellar, in spite of a slight saturation. This saturation produces a slight loss of event detection beyond the object in the direction of the TV line scanning (i.e. to its north). The saturation limit of the PCD on a given pixel depends on the count rate of the surrounding pixels. The input count rate recorded at the maximum of component A, 0.8–0.9 event per pixel per second, is near the limit of the maximum recordable count rate for an ideal point source illuminating a single pixel, 1 event per pixel per second (di Serego Alighieri, Perryman, and Macchetto 1985). The small size of component A (4 pixels FWHM), as well as inspection of the symmetry of the image, shows that this saturation affects the image of A on faint levels only and has therefore been neglected. (Another argument for assuming it is negligible is that image A has the same FWHM as unsaturated stellar objects in other exposures taken during the same night with equivalent exposure times). A second departure from linearity in the PCD comes from persistence effects; since these do not exceed a few percent (Llebaria *et al.* 1986), they have also been neglected here.

From atmospheric turbulence theory (Fried 1978; Hecquet and Coupinot 1985), the expected gain in resolution from recentering and selection techniques depends on the value of D/r_0, D being the size of the telescope and r_0 the Fried parameter (Fried 1966), the diameter of the diffraction-limited telescope having the resolution of the observations. The maximum gain is reached for D/r_0 between 3 and 5: it is ~2 for recentering only, and may reach a factor 3–4 after recentering *and* very stringent selection criteria (e.g., less than 10% of the images). Beyond $D/r_0 = 5$, i.e., for large telescopes in particular, the gain in resolution decreases rapidly. In the case of our observations, where short-integration exposures suggest an r_0 of ~20–25 cm at 3700 Å, D/r_0 is ~15–18, far from those values giving a maximum improvement. However, the atmosphere is not the only factor responsible for image degradation: dome (or local) seeing, as well as bad guiding and mechanical defects of the telescope can contribute in a nonnegligible manner. For instance, a factor of 2 has frequently been observed at the CFH telescope between "instant seeing" and the final resolution of a long-exposure image that should not arise from only the atmospheric image degradation (Nieto and Lelièvre 1981; Racine 1982). An illustration of this is the periodic features in the motion of a stellar image in both α and δ directions that were due to the imperfect telescope drive (Paper I). Because their amplitudes are 0".3 in α and 0".2 in δ, their effects are negligible for resolutions poorer than, say, 0".8, but contribute quite significantly to the image degradation when the target resolution is better than 0".5.

Two kinds of geometric distortion exist in the ESA PCD, which might affect any discussion concerning the geometry of the system. First, the S-distortion typical of magnetically focused intensifiers; second an imperfect perpendicularity between the horizontal and vertical scan directions. The large-scale S-distortion is negligible over the small field investigated. The correction for nonperpendicularity requires both a slight rotation (8°) and a 10% scale enlargement of the y-axis, necessary only for geometric purposes. This means a rebinning and then a slight smoothing of the images that inevitably produces a slight degradation of image quality. Therefore, we have

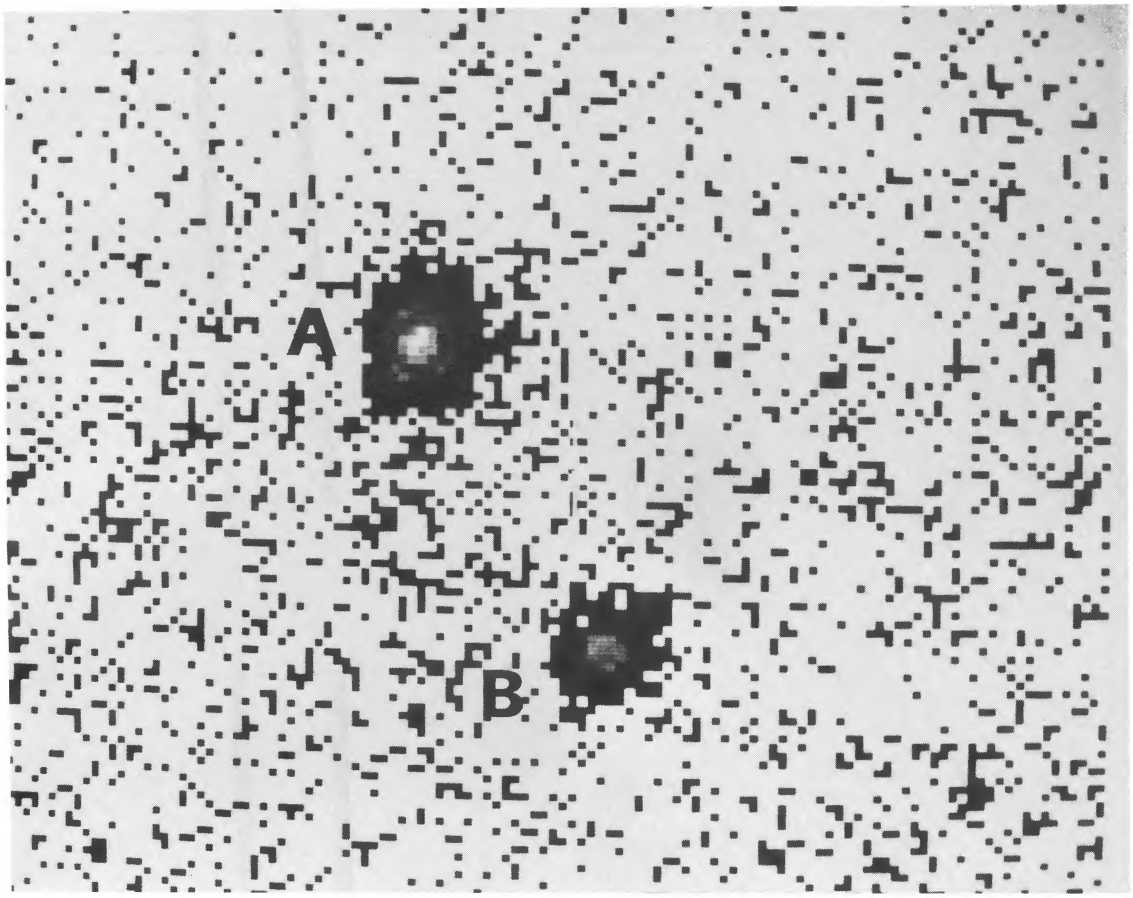

FIG. 1.—Integrated image obtained from the 100 s exposure No.4 showing the field of 2345 + 007 through a UG1 filter. The resolution is 0".53 (FWHM). The scale is given by the separation of the two components, 7".03. North on top: east at left.

NIETO *et al.* (*see* **325**, 645)

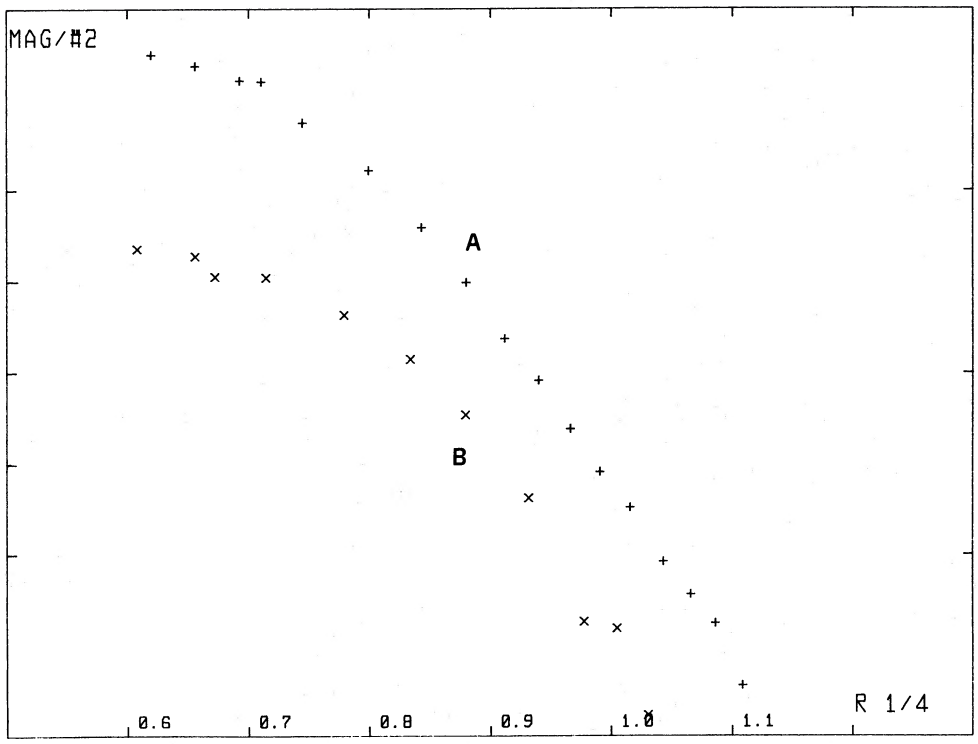

FIG. 2.—Light distribution (in a magnitude scale vs. $r^{1/4}$, with r in arcsec) of components A and B as derived from the sum of exposures 2, 3, and 4. The resolution is 0".63 (FWHM). The magnitude zero point is arbitrary.

chosen to analyze the raw images and have delayed as much as possible the correction for nonperpendicularity, performing this only at the last stage in the reduction procedure, for considerations on the geometrical configuration of the field. Otherwise, the one-dimensional equivalent light distribution of both objects A and B was obtained by measuring the area of the isophotal contours, S, from which the angular distance to the center is $r = (S/\pi)^{1/2}$. The mean scale of the two axes, e.g., 0".165 per pixel will be adopted for the conversion into arcseconds. All the following FWHMs were determined with this scale.

III. ANALYSIS OF INTEGRATED AND TRIM IMAGES

We measured independently the relative fluxes of components A and B on the integrated images as a test for variability. We obtained $U(\mathrm{A}) - U(\mathrm{B}) = 1.70 \pm 0.07$, 1.80 ± 0.02, and 1.78 ± 0.04 mag for exposures 1, 2 + 3 + 4, and 5, respectively. These values are in good agreement with that derived by Weedman *et al.* (1982) at 5200 Å, but differ significantly from those found by Sol *et al.* (1984) in the three U, B, and V bands, and by Tyson *et al.* (1986) in other colors.

As clearly visible on the total integrated images (e.g., Fig. 1) in spite of a slight image trail in the α direction (as visible in the central part of component A), component B appears resolved. On Figure 2, we have plotted the equivalent light profiles of both objects A and B from the sum of exposures No. 2, 3 and 4. We find $(\mathrm{FWHM})_A = 0".63$ and $(\mathrm{FWHM})_B = 0".80$. Exposures 1 and 5 confirm this result, and it has been verified that this cannot arise from the slight saturation of component A. In fact, if this saturation were not negligible, it would have introduced instead a loss of events in the center of component A, so that the difference between the central intensity of both components would actually be higher than that shown in Figure 2.

In the 2" × 2" window centered on component A, chosen to serve as the reference for image motion and quality (see Paper I), ~16 events per second were recorded. Since numerical simulations (Thouvenot 1987) show that a reliable recentering can only be obtained from component A with ~40 such events, the 30 ms frames were coadded to build up 2.5 s images and, for further checks, 8 s images.

A histogram of the resolutions of the 2.5 s exposure images constructed from coadded 30 ms frames and monitored during the 1000 s exposure of image No 4 is presented in Figure 3. This shows that 0".4 images can be derived with our procedure after recentering and (appropriate) selection.

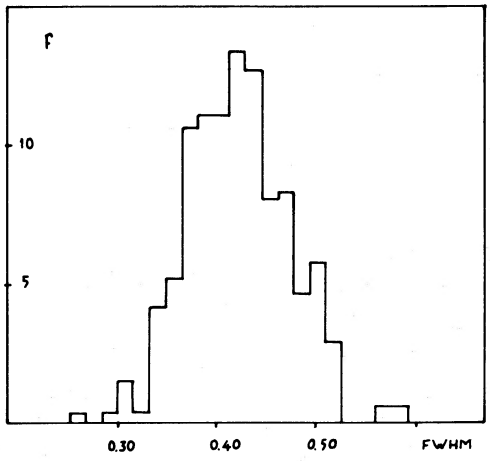

FIG. 3.—Distribution of the FWHM of component A for 2.5 s integration exposures, as determined from all events (including those from the sky) in a 2" × 2" window centered on A (see text).

TABLE 2

RESOLUTION[a] OF COMPONENT A ON RESULTING IMAGES[b]

MODE	OBSERVED IMAGES				RESTORED IMAGES
	Exposure 2	Exposure 3	Exposure 4	Sum	
Total:					
Integrated	0.61	0.60	0.53	0.63	0.26 (17.8)
Recentered	0.50	0.51	0.46	0.52	0.24 (14.5)
Recentered:					
+75% selection	0.48	0.49	0.46	0.47	0.26 (20.3)
+50% selection	0.47	0.47	0.43	0.45	0.28 (22.3)
+25% selection	0.45	0.47	0.40	0.43	...
+10% selection	(0.48)	0.44	0.39	0.40	...

[a] FWHM in arcsec.

[b] For restored images, the error estimate in percent is in parentheses.

Results of the recentering and selection techniques are summarized in Table 2, which gives the measured FWHM of component A for a 2.5 s integration time. Typical errors are $\pm 0''.01$ and increase to $\pm 0''.04$ for a 90% rejection rate. We show in Figure 4 the typical one-dimensional profiles for components A and B obtained from the image resulting from recentering and setting a 50% rejection rate on 2.5 s integration images. The resolution is $0''.45$. Typical images are presented in Figures 5*a* and 5*b* (Plates 23–24). Note that recentering removes the effects of guiding errors; the inner isophotes of component A are more circular than in Figure 1. Selection improves the resolution at the expense of a poorer signal-to-noise ratio. When recentering and selecting short-exposure images obtained with different integration times, the resolution of component A (used for reference) has greatly improved while that of component B, relatively, has not. This effect has been illustrated in Tables 2, 3, and 4 of Paper I: We have considered whether this could be due to the number of events used being too small for a reliable correction; however, the use of longer integration times (up to 20 s), and a correspondingly larger number of events did not remove this effect. These results also suggest that component B is "resolved" in such a way that the sharpening of the image does not strongly affect its size.

We also verified, by means of the 8 s binned data, that 2.5 s was not too short an integration time, in the sense that it might lead to overresolving the component used for correction, namely component A, relative to the other. As a further check we also applied these algorithms using component B. Unfortunately, as explained in Paper I and as shown by Thouvenot (1987), the contrast of component B above the sky is too low for reliable monitoring.

At this stage, the images were corrected for pixel distortion. We found that A and B are separated by $7''.03 \pm 0''.08$ a value in good agreement with the measurement by Sol *et al.* (1984),

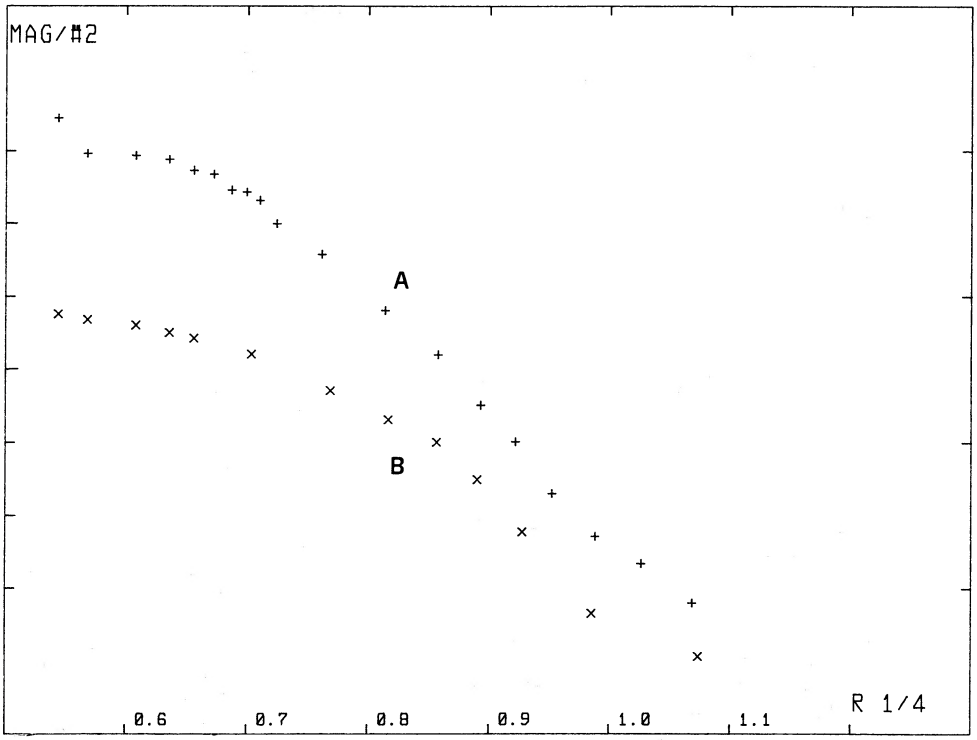

FIG. 4.—Light distribution (in a magnitude scale vs $r^{1/4}$, with r in arsec) of components A and B as derived from the sum of exposures 2, 3, and 4 after recentering and setting a 50% selection threshold of the 2.5 s integration images. The resolution of this image is $0''.45$(FWHM). The magnitude zero point is arbitrary.

PLATE 23

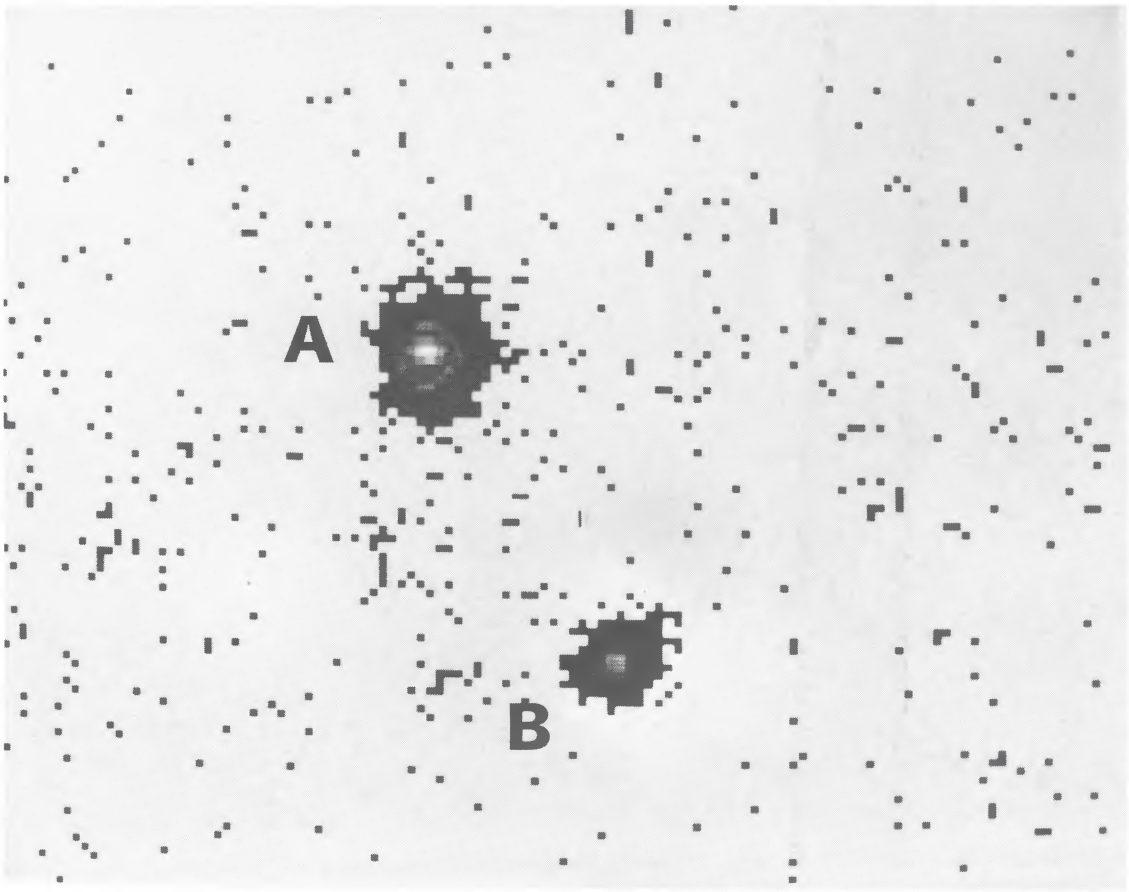

FIG. 5*a*.—Image resulting from recentering 2.5 s exposure images from exposure +4 without selection. The resolution is 0".46 (FWHM). Same orientation and scale as in Fig. 1.

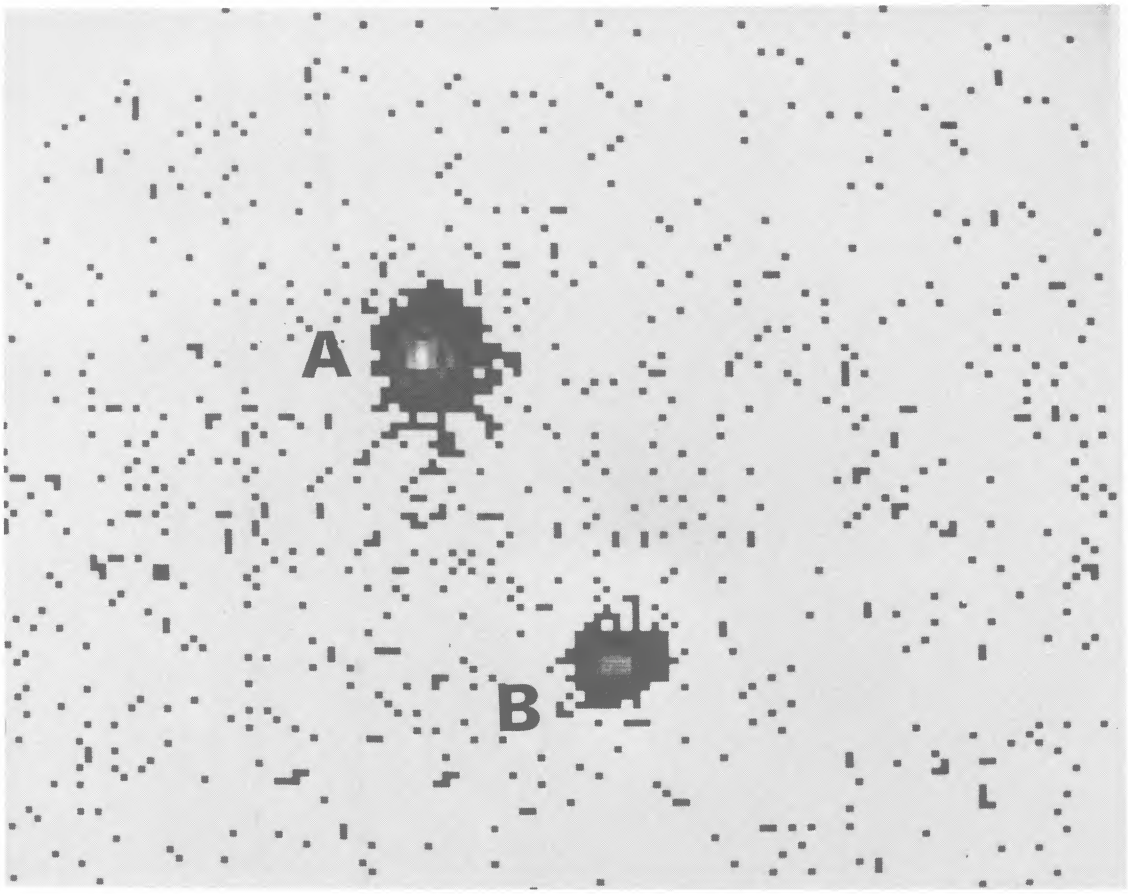

FIG. 5*b*.—Image resulting from recentering 2.5 s exposure images with a 25% selection rate from exposure +4. The resolution is 0".40 (FWHM). Same orientation and scale as in Fig. 1.

although significantly smaller than the usually quoted value of 7".3. We also determined that the position angle of the AB direction is 57° ± 1°, The position angle of the major axis of component B was determined on two total integrated images (Nos. 2+3+4 and 5) by computing the second moment of the best ellipse fitting the surface located within isophotal contours (Prugniel 1988; Prugniel, Nieto, and Simien 1987). We found P.A. = 135° ± 2°; hence the elongation of component B makes an angle of ~80° with the AB direction.

IV. IMAGE RESTORATION OF COMPONENT B

Image restoration algorithms have also been used in order to extract the best image from the different images obtained above. One of the main problems with such algorithms is the reliability of the reconstruction procedures. Details on our deconvolution method is given in Lannes, Roques and Casanove (1987), Lannes, Casanove, and Roques (1987), and Roques (1987).

It is based on the principle that it is not possible to restore fully the original object and that only a smoothed version of the original object can be reconstructed: once a given target resolution is decided for the restored image, this image is obtained with an estimate of its relative quadratic error. This estimate is based, in particular, on an analysis of the noise attached to the original image. We chose a Gaussian representation of this noise; from a theoretical point of view, it is a compound Poisson noise, but the large number of events, as well as the image characteristics, led us to adopt a Gaussian representation. This hypothesis is in fact very conservative, since it yields an error estimate higher than what a Poissonian noise would have given. Based on the values of the signal-to-noise ratio at each point in the frequency plane, different weights are given to the corresponding spectral information. The spectral decomposition (in eigenvalues and eigenvectors) of the operator characterizing these weights is of particular importance in the study of the errors: the eigenvalues appear in the calculation of the relative error of the reconstruction, while the behaviors of the eigenvectors allow us to verify that the details appearing in the reconstruction are not artifacts. Practically, the reconstruction is implemented in an interactive manner with the conjugate gradients method (Murray 1972); this method leads to the least-squares solution in ~10 iterations.

These algorithms were applied to four images resulting from the recentering and selection algorithms applied to exposures 2, 3, and 4 altogether, adopting a 2.5 s integration time. Because of the poor signal-to-noise ratio in the images resulting from stringent selection rates, only the 75% and the 50% selection images were considered. The restored images, shown in Figure 6, were obtained in about six iterations. Their

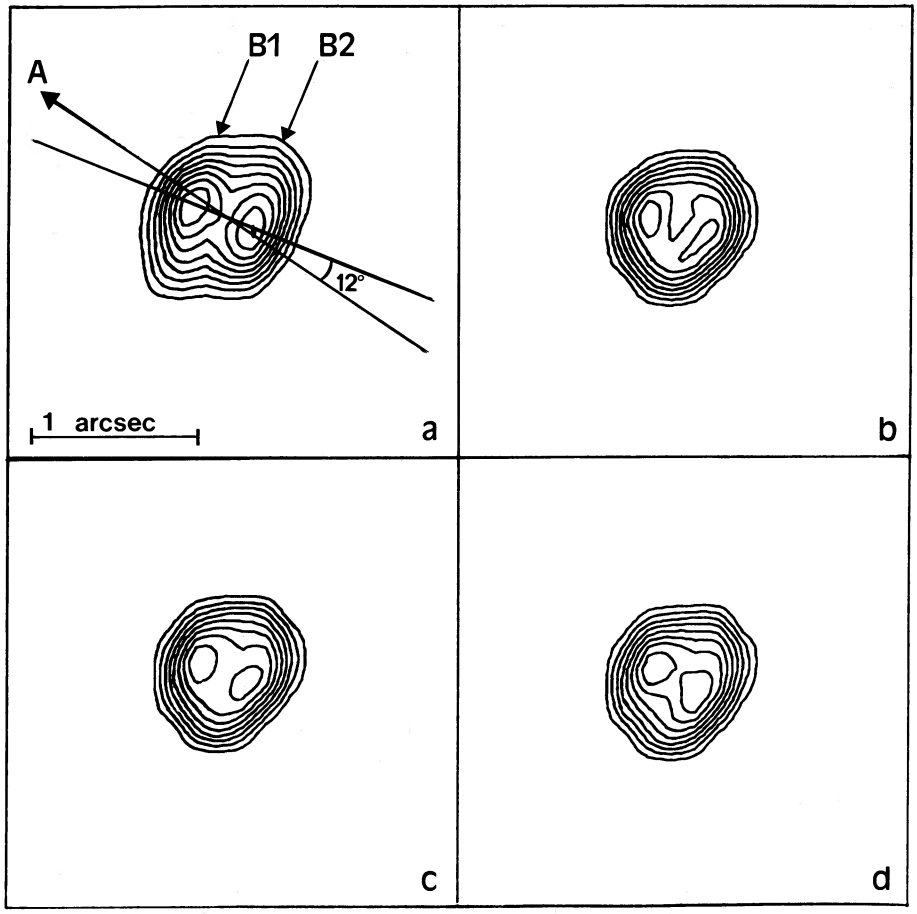

FIG. 6.—Isophotal contours (separated by constant intensities) of the restored images of component B from images derived from the algorithms applied to exposures 2, 3, and 4 altogether. (*a*) From the integrated image (*b*), (*c*), and (*d*) from recentering and different selection thresholds. Resolutions (FWHM) and error estimates are, respectively (*a*) 0".26 and 17.8% (*b*) 0".24 and 14.5%; (*c*) 0".26 and 20.3%; (*d*) 0".28 and 22.3%. The direction of component A is indicated with an arrow making a 12° angle with the B1–B2 direction. Same orientation as in Figs. 1 and 5.

resolutions and the estimate of the quadratic errors attached to them are given in Table 2, columns (5) and (6).

The best image derived from this procedure is certainly that obtained from the recentered one with no selection, where the resolution reached is 0".24 with a (conservative) quadratic error estimate of 14%. Accepting a slightly higher error estimate (such as for the other restored images) would have yielded an even better resolution. Restoration applied to the recentered image benefits with regard to the integrated one from not only a better starting resolution but also from a rounder shape of the stellar profile used in the deconvolution procedure. The two images resulting from both recentering and selection, although starting from a slightly better resolution, suffer from a poorer signal-to-noise ratio.

The image restoration procedure demonstrates in all resulting images that component B is divided into two components, B1 and B2, that are 0".36 apart, and almost aligned with the AB direction: the line of their centers (P.A. = 69°) makes an 12° angle with the AB direction. Although small, this angle is significantly different from zero. At least one component, B2, appears elongated (see e.g., Fig. 6*b*): this is shown not only by the shape of the isophotes, but also by the size of the faintest one along the direction of the elongation, 1".05. Because of the error attached to our deconvolved images, there is no evidence for B1 being elongated. Its slight apparent elongation is probably due to blurring with component B2. Therefore, the elongation of B that we have detected on the unrestored images appears to be due to two contributions: one is the presence of two subcomponents, B1 and B2, and the other is the elongation (at the 0".25 resolution) of B2.

The two subcomponents seem to have roughly equal fluxes. Because of their blending, we did not attempt to measure their relative fluxes.

In addition, we note that both the elongation of component B and the existence, after image restoration, of two substructures, B1 and B2 (elongated), has been confirmed on 0".6–0".7 CCD data obtained in the V band at the Cassegrain focus of the CFH telescope.

V. PHYSICAL INTERPRETATION

From the results obtained above, it is tempting to believe that B2 is an elongated galaxy on the line of sight of the system, while B1 is a pure image of the source quasar. However, the observed geometry makes it extremely unlikely that B2 could be responsible for the splitting between A and B1, even with the help of an associated cluster.

Moreover, B2 cannot be simply a galaxy since, the fluxes of B1 and B2 being roughly equal in the UV band, component B as a whole would be much redder than measured so far (see Sol *et al.* 1984; Tyson *et al.* 1986) if B2 were a normal galaxy at any redshift between 0 and 2. Indeed the absence of conspicuous deflecting body (galaxy or cluster) leads us to assume that its redshift would be quite high, perhaps ~ 1.5 as suggested by the absorption lines detected in the spectra of A and B (Foltz *et al.* 1984). The slightly redder color [$\Delta(B-I) \approx 0.1$] of component B relative to A implies that the contribution of a galaxy at this redshift would be smaller than 10% in the I band and probably much less than 2% in the U band. Furthermore, the equivalent widths of the emission lines also seem to rule out a large contribution of a galactic continuum in the spectrum of component B. In fact, the equivalent width difference observed by Weedman *et al.* (1982) is in the "wrong" sense and could be attributed to galactic contamination of component A, and/or to intrinsic variation of the continuum of the source quasar, combined with time delay effect.

We conclude that subcomponent B2 is better interpreted as an unresolved multiple component image of the source than a really extended object.

Subcomponents B1 and B2 are probably not the second and third images expected, in addition to A, from a single deflector when the source position is near a critical curve. Such a pair would be much brighter, as observed for components A1 and A2 in the case of the "triple" quasar PG 1115+080. Thus, it is almost impossible to escape the conclusion that several galaxies are involved in the lensing and that component B is a complex of at least three images of the quasar possibly mixed with a very faint galaxy.

A coherent model could be the following:

A, B1, and B2 are different images of the same source quasar, with B2 having probably some substructure. The A–B splitting would result from the combined action of a galaxy at $z \approx 1.5$ and its cluster as a whole, involving possibly "dark" matter (Tyson *et al.* 1986), while the B1–B2 splitting requires the action of a second galaxy in the same cluster, this galaxy being possibly that contributing to B2. The existence of two absorption systems in the spectrum of B, with $\Delta v \approx 1000$ km s^{-1} (Foltz *et al.* 1984) supports this interpretation. The second galaxy would have a mass of the order of $5 \times 10^{10}\ M_{\odot}$ to account for the observed 0".36 splitting between B1 and B2 (calculated with $H_0 = 50$ km s^{-1} Mpc^{-1} and $q_0 = \frac{1}{2}$). Its apparent magnitude would be $m_v \approx 25$, well within observational limits. The substructure of B2 could easily result from the complexity of the deflecting system. Further investigations in several colors are evidently required before any detailed model could be reasonably built.

We would finally like to comment on the puzzling "alignment" of A, B1 and B2 (although, as commented by the referee, 12° is not too astounding a coincidence): since B2 cannot be responsible for the A-B splitting, we must conclude that this alignment is fortuitous.

VI. CONCLUSION

The substructures found in component B strongly support the gravitational lens hypothesis. They unavoidably call for further high-resolution imaging observations, notably in the red, in order to understand the nature of the different subcomponents. Speckle interferometry observations would be even more informative, but, because of the faintness of the different components, they would require exceptionally good observing conditions (see Foy, Bonneau, and Blazit 1985). At longer wavelengths, in principle, high-resolution imaging should be easier to achieve since resolution increases (although not strongly) with wavelength for given atmospheric conditions.

In fact, the resolution that we have reached in this study is far from being the best possible that can be achieved from the ground. As discussed earlier, the data recorded were not really appropriate for reaching the highest resolution. For instance, the pixel size was too large with regard to the resolution achieved, and the integration time was too long to monitor the short-scale atmospheric time variations. As discussed in Paper I, these two problems could easily be solved by working at longer focal lengths. On the other hand, as shown in Lelièvre *et al.* (1987), pupil segmentation can optimize this approach by recording lower D/r_0 images, yielding, after recentering and

selection and before any restoration procedures, a resolution of 0".20–0".25.

Last, but not least, this approach would obviously be improved with substantially larger observing times. In the present study, we showed that the improvement in resolution obtained from image selection could not compensate the loss in signal-to-noise ratio, so that the whole strategy could not give its maximum improvements: the best restored images turned out to come from the recentered one. This has two causes: the inappropriate observing conditions already mentioned (too long integration time, too high D/r_0, etc.), preventing a large improvement in resolution through selection, and also a limited total exposure time. It is likely that even with similar observing conditions, but with a total exposure time a few times longer, the resolution of restored images could have reached 0".2 or better.

REFERENCES

Bahcall, J. N., Bahcall, N. A., and Schneider, D. P. 1986, *Nature*, **323**, 515.
Banse, K., Crane, Ph., Ounnas, Ch., and Ponz, J. D. 1983, *Proc. DECUS*, (Zurich), p. 87.
di Serego Alighieri, S., and Perryman, M. A. C. 1986, *Proc. SPIE*, **627**, 201.
di Serego Alighieri, S., Perryman, M. A. C., and Macchetto, F. D. 1985, *Astr. Ap.*, **149**, 179.
Foltz, C. B., Weymann, R. J., Röser, H. J., and Chaffee, F. H. 1984, *Ap. J. (Letters)*, **281**, L1.
Fort, B., Picat, J.-P., Cailloux, M., Mauron, N., Dreux, M., and Fauconnier Th. 1984, *Astr. Ap.*, **135**, 356.
Foy, R., Bonneau, D., and Blazit, A. J. 1985, *Astr. Ap.*, **149**, L13.
Fried, D. L. 1966, *J. Opt. Soc. Am.*, **56**, 372.
———. 1978, *J. Opt. Soc. Am.*, **68**, 1651.
Hecquet, J., and Coupinot, G. 1985, *J. Optics*, **16**, 21.
Lannes, A., Casanove, M.-J., and Roques, S. 1987, *J. Mod. Optics*, **34**, 321.
Lannes, A., Roques, S., and Casanove, M.-J. 1987, *J. Mod. Optics*, **34**, 161.
Lelièvre, G., Nieto, J.-L., Salmon, D., Llebaria, A., Thouvenot, E., Boulesteix, J., Lecoarer, E., and Arnaud, J. 1987, *Astr. Ap.*, in press.
Llebaria, A., Nieto, J.-L., and di Serego Alighieri, S. 1986, *Astr. Ap.*, **168**, 389.
Murray, W. 1972, *Numerical Methods for Unconstrained Optimization* (New York: Academic).
Nieto, J.-L., and Lelièvre, G. 1981, *Astronomical Photography 1981*, ed. J.-L. Heudier and M. E. Sim (CNRS-INAG), p. 189.
———. 1985, in *Lecture Notes in Physics*, Vol. **232**, *New Aspects of Galaxy Photometry* ed. J.-L. Nieto (Berlin: Springer), p. 43.
Nieto, J.-L., Llebaria, A., and di Serego Alighieri, S. 1987, *Astr. Ap.*, **178**, 301 (Paper I).
Prugniel, Ph. 1988, Thèse d'Etat, Université Paul Sabatier, Toulouse.
Prugniel, Ph., Nieto, J.-L., and Simien, F. 1987, *Astr. Ap.*, **173**, 49.
Racine, R. 1982, private communication quoted in Fort *et al.* (1984).
Roques, S. 1987, Thèse d'Etat, Université Paul Sabatier, Toulouse.
Sol, H., Vanderriest, Ch., Lelièvre, G., Pedersen, H., and Schneider, J. 1984, *Astr. Ap.*, **132**, 105.
Subramanian, K., and Chitre, S. J., 1984, *Ap. J.*, **276**, 440.
Thompson, L. A. 1984, *Ap. J. (Letters)*, **279**, L47.
Thompson, L. A., and Ryerson, H. R. 1983, *Proc. SPIE*, **445**, 560.
Thouvenot, E. 1987, Stage de DEA, Université Paul Sabatier, Toulouse.
Tyson, J. A., Seitzer, P., Weymann, R. J., and Foltz, C. 1986, *A.J.*, **91**, 1274.
Walsh, D., Carswell, R., and Weymann, R. 1979, *Nature*, **279**, 381.
Weedmann D. W., Weymann, R. J., Green, R. F., and Heckman, T. M. 1982, *Ap. J. (Letters)*, **255**, L5.

S. DI SEREGO ALIGHIERI: The Space Telescope European Coordinating Facility, Karl Schwarzschild Strasse 2, 8046 Garching bei München, Federal Republic of Germany

G. LELIÈVRE: Canada-France-Hawaii Telescope Corporation, P.O. Box 1597, Kamuela, HI 96743

A. LLEBARIA: Laboratoire d'Astronomie Spatiale, Traverse du Syphon, Les Trois Lucs, 13004 Marseille, France

F. D. MACCHETTO: Space Telescope Science Institute, 3700 San Martin Drive, Homewood Campus, Baltimore, MD 21218

J.-L. NIETO and S. ROQUES: Observatoire du Pic du Midi et de Toulouse, 14, Avenue Edouard Belin, 31400 Toulouse, France

M. A. C. PERRYMAN: European Space Agency, ESTEC, Postbus 299, 2200 AG Noordwijk, The Netherlands

CH. VANDERRIEST: Observatoire de Meudon, 92195 Meudon Principal Cedex, France